

LETTER TO THE EDITOR

Discovery of two metallic cyanoacetylides in IRC+10216: HMgCCCN and NaCCCN[★]

C. Cabezas¹, J. R. Pardo¹, M. Agúndez¹, B. Tercero^{2,3}, N. Marcelino^{2,3}, Y. Endo⁴, P. de Vicente³, M. Guélin⁵,
J. Cernicharo¹

¹ Departamento de Astrofísica Molecular, Instituto de Física Fundamental (IFF-CSIC), C/ Serrano 121, 28006 Madrid, Spain
e-mail: carlos.cabezas@csic.es & jose.cernicharo@csic.es

² Centro de Desarrollos Tecnológicos, Observatorio de Yebes (IGN), 19141 Yebes, Guadalajara, Spain

³ Observatorio Astronómico Nacional (OAN, IGN), Madrid, Spain

⁴ Department of Applied Chemistry, Science Building II, National Yang Ming Chiao Tung University, 1001 Ta-Hsueh Rd., Hsinchu 300098, Taiwan

⁵ Institut de Radioastronomie Millimétrique, 300 rue de la Piscine, F-38406, Saint Martin d'Hères, France

Received; accepted

ABSTRACT

We report on the detection of a series of six lines in the ultra-deep Q-band integration toward IRC +10216 carried out with the Yebes 40m telescope, which are in harmonic relation with integer quantum numbers J_u from 12 to 18. After a detailed analysis of all possible carriers, guided by high-level quantum chemical calculations, we conclude that the lines belong to HMgCCCN, named hydromagnesium cyanoacetylide. The rotational temperature and column density derived for HMgCCCN are 17.1 ± 2.8 K and $(3.0 \pm 0.6) \times 10^{12}$ cm⁻², respectively. The observed abundance ratio between MgCCCN and HMgCCCN is ~ 3 . In addition, we report the discovery in space, also toward IRC +10216, of sodium cyanoacetylide, NaCCCN, for which accurate laboratory data are available. For this species we derive a rotational temperature of 13.5 ± 1.7 K and a column density of $(1.2 \pm 0.2) \times 10^{11}$ cm⁻².

Key words. molecular data – line: identification – ISM: molecules – ISM: individual (IRC +10216) – astrochemistry

1. Introduction

Metal-containing molecules are almost exclusively found in space toward circumstellar envelopes around evolved stars, except for a few recent detections toward protostars (Ginsburg et al. 2019; Tachibana et al. 2019). Most of these molecules have been discovered toward IRC+10216 the carbon-rich envelope of the star CW Leo. The first metal-bearing molecules detected in IRC +10216 were diatomic halides such as NaCl, KCl, AlCl, and AlF (Cernicharo & Guélin 1987). These species are formed in the hot inner parts of the envelope, close to the AGB star. The discovery and mapping of MgNC (Kawaguchi et al. 1993; Guélin et al. 1993) revealed that metal-bearing molecules are also formed in the cool outer regions of the envelope. Other metal cyanides and isocyanides, such as NaCN (Turner et al. 1994), MgCN (Ziurys et al. 1995), AlNC (Ziurys et al. 2002), KCN (Pulliam et al. 2010), FeCN (Zack et al. 2011), HMgNC (Cabezas et al. 2013), and CaNC (Cernicharo et al. 2019a), were later on detected in the same source and are probably formed in the cool outer regions of the envelope. Indeed, metal atoms have been observed to survive in the gas phase in these regions (Mauron & Huggins 2010), allowing for the formation of these metal-bearing molecules, specially those containing magnesium. Indeed, a variety of Mg-containing carbon chains of increasing length, such as MgC₂, MgCCH, MgC₄H, MgC₆H, MgC₃N, and

MgC₅N, have been recently detected (Agúndez et al. 2014; Cernicharo et al. 2019b; Pardo et al. 2021; Changala et al. 2022).

In this letter we present the discovery in space of two new metal-bearing carbon chains toward IRC +10216. These molecules are HMgCCCN, a further member of the family of Mg-bearing molecules, and NaCCCN, the first long carbon chain of the family of Na-bearing molecules. These two molecules were detected thanks to a deep integration in the Q band (31.0–50.3 GHz) with the Yebes 40m telescope. The identification of HMgCCCN is based on high-level quantum chemical calculations while that of NaCCCN relies on previous laboratory data (Cabezas et al. 2019). In addition, we provide an upper limit to the abundance of the aluminum cyanoacetylide, AlCCCN, in IRC +10216.

2. Observations

New receivers, built within the Nanocosmos¹ project and installed at the Yebes 40m radiotelescope, were used for the observations of IRC +10216 ($\alpha_{J2000} = 9^{\text{h}}47^{\text{m}}57.36^{\text{s}}$ and $\delta_{J2000} = +13^{\circ}16'44.4''$) as part of the Nanocosmos survey of evolved stars (Pardo et al. 2022). Data from the QUIJOTE² line survey (Cernicharo et al. 2021a, 2022, 2023) toward TMC-1 were also used to discriminate between possible carriers of the lines found in IRC +10216.

[★] Based on observations carried out with the Yebes 40m telescope (projects 19A010, 20A017, 20B014, 21A019). The 40m radio telescope at Yebes Observatory is operated by the Spanish Geographic Institute (IGN, Ministerio de Fomento).

¹ ERC grant ERC-2013-Syg-610256-NANOCOSMOS.

<https://nanocosmos.iff.csic.es/>

² Ultrasensitive Inspection Journey to the Obscure TMC-1 Environment

Table 1. Observed line parameters of HMgCCCN and NaCCCN toward IRC +10216.

Transition J_u-J_l	ν_{obs}^a (MHz)	$\nu_{obs} - \nu_{cal}^b$ (MHz)	$\int T_A^* dv^c$ (mK km s $^{-1}$)	$T_A^*(horn)^d$ (mK)	$T_A^*(center)^e$ (mK)	Notes
HMgCCCN						
12-11	31672.704±0.050	0.0569	39.84	1.48	1.31	A
13-12	34311.875±0.050	-0.0304	38.53	1.45	1.26	
14-13	36951.092±0.050	-0.0407	42.28	1.59	1.39	
15-14	39590.327±0.020					B
16-15	42229.489±0.050	0.0040	53.36	2.06	1.72	C
17-16	44868.617±0.050	0.0118	50.25	2.22	1.48	
18-17	47507.686±0.050	0.0010	72.11	3.06	2.19	
19-18	50146.722±0.040					≤3.5, D
NaCCCN						
12-11	31705.51±0.20	-0.0447	13.25	0.49	0.44	
13-12	34347.56±0.30	0.0147	11.35	0.43	0.37	E
14-13	36989.38±0.20	-0.1235	12.17	0.46	0.40	
15-14	39631.36±0.20	-0.0667	11.35	0.44	0.37	
16-15	42273.31±0.20	-0.0024	10.64	0.41	0.34	
17-16	44915.22±0.40	0.0619	17.38	0.77	0.51	F
18-17	47556.89±0.40	-0.0709	17.67	0.75	0.54	

Notes.

^(a) Observed frequency assuming a $V_{LSR} = -26.5$ km s $^{-1}$. ^(b) Observed minus calculated frequencies in MHz. ^(c) Integrated line intensity in mK km s $^{-1}$. The total uncertainty is assumed to be dominated by the calibration uncertainties of 10%. ^(d) Antenna temperature at the terminal velocity (horn) in mK. ^(e) Antenna temperature at line center in mK. ^(A) Line partially blended with a weak hyperfine component of CC 13 CH. Frequency and line parameters can be correctly estimated adopting the observed intensities of the other hyperfine components of CC 13 CH (see top panel of Fig. 1). ^(B) Line fully blended with C $_3$ N. Frequency and line parameters cannot be estimated. The quoted frequency corresponds to the predicted one. ^(C) Line partially blended with *c*-C $_3$ H $_2$. Frequency and line parameters can still be estimated. ^(D) Line not detected. The upper limit in antenna temperature corresponds to 3σ . The quoted frequency corresponds to the predicted one. ^(E) Line partially blended with an unknown feature. Frequency and line parameters can still be estimated. ^(F) Line blended with an unknown feature and with a line from HC $_9$ N in the $3\nu_{19}$ state. Frequency and line parameters are very uncertain.

A detailed description of the telescope, receivers, and backends can be found in Tercero et al. (2021). Briefly, the receiver consists of two cold high electron mobility transistor amplifiers covering the 31.0-50.3 GHz band with horizontal and vertical polarizations. Receiver temperatures range from 16 K at 31 GHz to 25 K at 50 GHz. The backends are $2 \times 8 \times 2.5$ GHz fast Fourier transform spectrometers with a spectral resolution of 38.15 kHz, providing the whole coverage of the Q band in both linear polarizations. The data were smoothed to 228.9 kHz (six channels), which corresponds to a velocity resolution of 1.7 km s $^{-1}$ at 40 GHz. This spectral resolution is good enough to resolve the broad U-shaped lines of IRC +10216 which exhibit a full velocity width of 29 km s $^{-1}$ (Cernicharo et al. 2000). The intensity scale used in this work, antenna temperature (T_A^*), was calibrated using two absorbers at different temperatures and the atmospheric transmission model ATM (Cernicharo 1985; Pardo et al. 2001). Calibration uncertainties were adopted to be 10%. Additional uncertainties could arise from the line intensity fluctuation with time induced by the variation of the stellar infrared flux (Cernicharo et al. 2014; Pardo et al. 2018). The beam efficiency of the Yebes 40m telescope in the Q band is given as a function of frequency by $B_{eff} = 0.797 \exp[-(\nu(\text{GHz})/71.1)^2]$ and the forward telescope efficiency is 0.97. The emission size is assumed to have a radius of 15 arcsec, as observed for MgNC IRC+10216 (Guélin et al. 1993). Pointing corrections were obtained by observing the SiO masers of R Leo. Pointing errors were always within 2-3". All data were analyzed using the GILDAS package³.

3. Results

Our current data of IRC +10216 have never before reached a sensitivity (σ) as low as 0.15 mK at some frequencies in the T_A^* scale for a spectral resolution of 229 kHz. This exceptional data quality has already been shown in recent publications presenting the detection of MgC $_5$ N and MgC $_6$ H (Pardo et al. 2021), and of C $_7$ N $^-$ (Cernicharo et al. 2023). The data show a large number of lines coming from isotopologues and vibrationally excited states of abundant species that are identified using the catalogues MADEx (Cernicharo 2012), CDMS (Müller et al. 2005), and JPL (Pickett et al. 1998).

In order to derive line parameters we use the SHELL method of the GILDAS package, which is well adapted for the line profiles observed in circumstellar envelopes. A variable window of 50-100 MHz around the line centre is used in this process. In all cases we fix the terminal expansion velocity of the envelope to 14.5 km s $^{-1}$ (Cernicharo et al. 2000).

3.1. Identification of HMgCCCN

Among the unidentified lines that arise with high signal-to-noise ratio in the current Q-band spectrum of IRC +10216, six of them are in harmonic relation from $J_u=12$ to $J_u=18$. They were reported as unidentified features in the previous, much noisier, published version of the survey (Pardo et al. 2022). The lines are shown in Fig. 1 and the line parameters are provided in Table 1. Most of the observed lines of this series are free of blending, except the $J=15-14$ which is fully blended with C $_3$ N. Two of them ($J=13-12$ and $J=16-15$) have a marginal overlap with another feature but line fit is still possible. The lines do not show any evidence for spectroscopic broadening due to fine and/or hyperfine structure. They can be fitted to a standard line profile for an ex-

³ <http://www.iram.fr/IRAMFR/GILDAS>

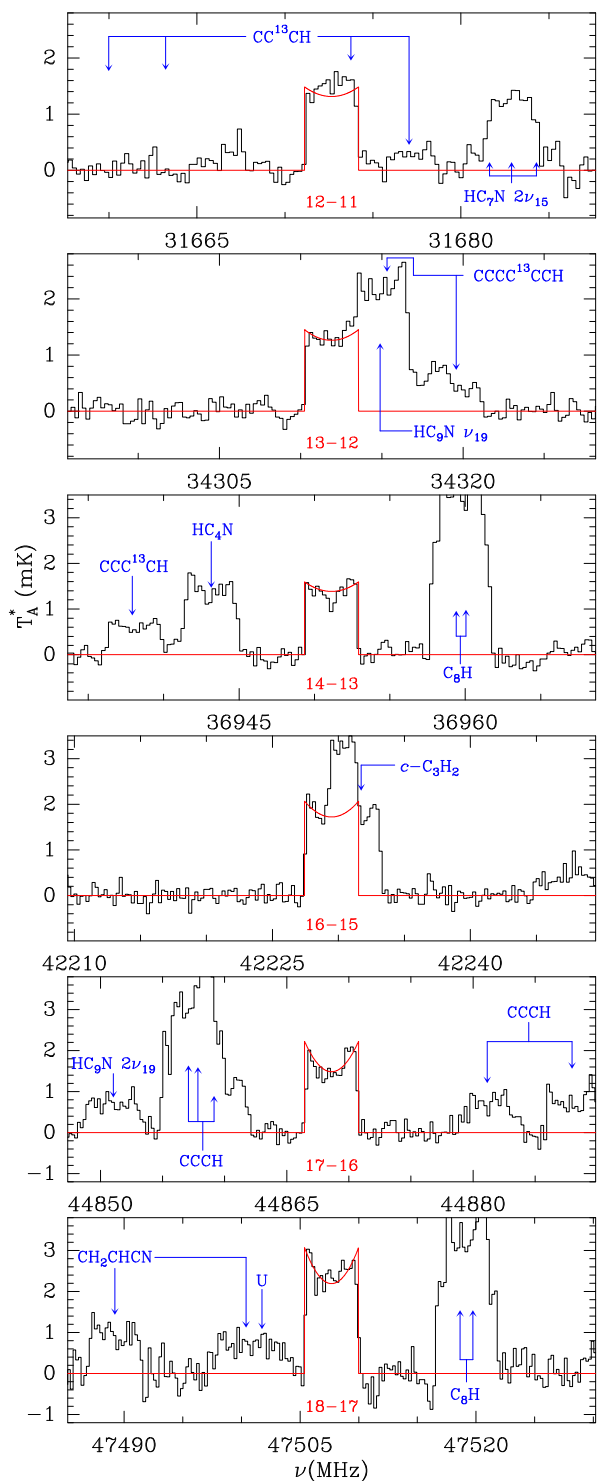


Fig. 1. Lines of HMgCCCN observed with the Yebes 40m telescope toward IRC +10216. Line parameters are given in Table 1. The abscissa corresponds to the rest frequency assuming a local standard of rest velocity of -26.5 km s^{-1} . The ordinate is the antenna temperature corrected for atmospheric and telescope losses in mK. The red lines show the fitted line profiles adopting an expanding terminal velocity of 14.5 km s^{-1} (Cernicharo et al. 2000).

panding envelope with a terminal expansion velocity of 14.5 km s^{-1} (Cernicharo et al. 2000). Hence, the carrier of the lines has a $^1\Sigma$ ground electronic state. The lines can be fitted to the standard Hamiltonian of a linear rotor providing the spectroscopic constants shown in Table 2. We name this carrier as B1320. We

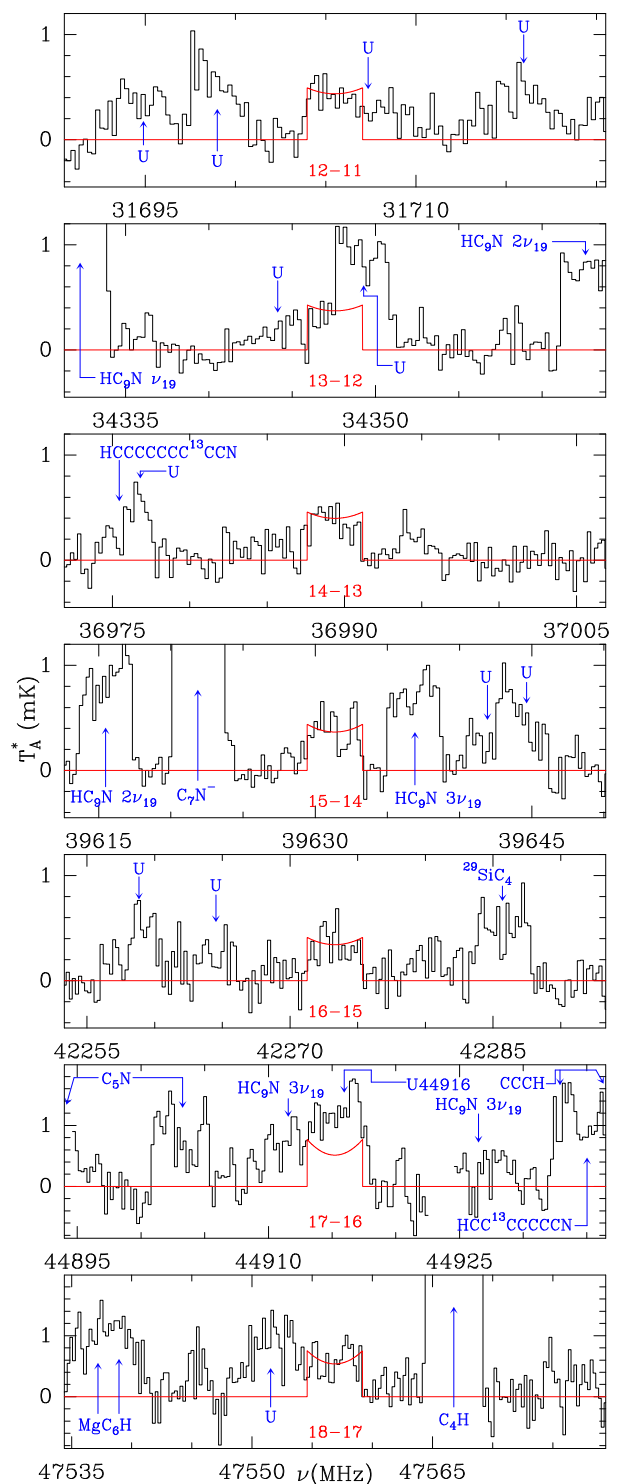


Fig. 2. Same as Fig. 1 but for NaCCCN.

checked that values of B divided by integers ranging from 2 to 6 do not match the observations as many lines would be missing.

The derived rotational constant is close to that of HC₅N (1331.333 MHz). All the isotopologues of this species can be discarded since they have already been reported in this source (Pardo et al. 2022). In addition, all possible isomers of HC₅N have rotational constants larger than that of B1320 (Cernicharo et al. 2020a). Other potential species could be the isotopologues of the anions C₆H⁻ and C₅N⁻, which have rotational constants B of 1376.8630 MHz and 1388.8673 MHz, respectively. However,

the intensities of C_6H^- in our survey are 10-15 mK, and those of C_5N^- are 4-6 mK. Hence, all the isotopologues of these species will have intensities well below the mK level, thus undetectable at the current level of sensitivity. Moreover, the distortion constants for all these possible candidates are around 30 Hz which is a factor of three lower than that of B1320. Distortion constants as large as the observed one are only provided by molecules containing a metal. Some species containing Si could have rotational constants around the observed value. For example SiC_4 has a rotational constant of 1510 MHz and exhibits lines of 10-15 mK in the Q-band. All its isotopologues have been observed in the laboratory and none matches the rotational constant of B1320. Species such as $SiCCCN$ (Umeki et al. 2014) or $CCCCS$ (Hirahara et al. 1993) are open-shell species and cannot be considered as potential carriers.

AICCCN and NaCCCN have been observed in the laboratory and have rotational and distortion constants similar to those found for B1320. NaCCCN has been detected in this work (see Section 3.2), and all its possible isomers have rotational constants larger than that of B1320 (Cabezas et al. 2019). The intensities of the NaCCCN lines are 2-3 times lower than those of B1320. Although the rotational constants of the NaCCCN isotopologues could be close to that of B1320, the expected intensities are too low to match those observed for B1320. AICCCN is not detected at the present level of sensitivity and its isomers, similar to NaCCCN, have too large rotational constants. Hence, we have to consider another metal such as Mg for which several species containing it have been detected in IRC +10216. Ab initio calculations by Cabezas et al. (2014, 2019) exclude also other possibilities such as molecules containing Ca.

Taking into account that MgCCCN and MgCCCCH are both detected in IRC +10216 with column densities of $\sim 10^{13} \text{ cm}^{-2}$ (Cernicharo et al. 2019b; Pardo et al. 2021), we proceed in our search with high level ab initio calculations for their hydrogenated counterparts HMgCCCN and HMgCCCCH using the same level of calculation as in previous studies (Cernicharo et al. 2019b): CCSD(T)-F12 (Knizia et al. 2009) with all electrons (valence and core) correlated and the Dunning's correlation consistent basis sets with polarized core-valence correlation triple- ζ for explicitly correlated calculations (cc-pCVTZ; Hill et al. 2010). All the calculations were carried out using the Molpro 2020.2 program (Werner et al. 2020). The calculated rotational constants for the two species are very similar: 1319.1 MHz and 1319.3 MHz for HMgCCCN and HMgCCCCH, respectively. However, the low dipole moment of 0.3 D calculated for HMgCCCCH excludes it as a possible carrier because a column density as high as $\sim 8 \times 10^{14} \text{ cm}^{-2}$ would be needed to reproduce the observed intensities. In contrast, the dipole moment calculated for HMgCCCN is 4.5 D, which makes it the best candidate for B1320. The centrifugal distortion constant D calculated at the same level of theory for HMgCCCN is 62.1 Hz, a bit different from the one derived in our fit. However, the hydromagnesium derivatives are more floppy molecules, due to the HMgC bending mode, than the non-hydrogenated analogues and the prediction of this parameter is less reliable (Cernicharo et al. 2019b; Pardo et al. 2021). This is also seen for HMgNC, whose D value is 2.94 kHz, while the one calculated using the mentioned level of calculation is 2.3 kHz. We used this experimental/theoretical ratio to scale the theoretical value of D for HMgCCCN with the result of 79.0 Hz, which is closer to the one derived from our astronomical data considering 3σ uncertainty of the experimental value. It must be said that we obtained a reliable fit also keeping D constant fixed to 79.0 Hz. From the observed line intensities of HMgCCCN we derive a rotational temperature of $17.1 \pm 2.8 \text{ K}$ and a column

Table 2. Spectroscopic parameters of HMgCCCN

Parameter	Astronomical	Theoretical ^a
B / MHz	1319.7222 \pm 0.0021	1319.1
D / Hz	99.2 \pm 4.1	79.0 ^b
rms / kHz	38.7	
μ / D		4.5

Notes.

^(a) Calculations from this work (see text). ^(b) Value corrected using the experimental/theoretical D ratio of HMgNC (see text).

Table 3. Spectroscopic parameters of NaCCCN.

Parameter	Lab + IRC +10216 ^a	Laboratory ^b
B / MHz	1321.094464(27) ^c	1321.094334(28)
D / Hz	104.83(56)	101.1(7)
$eQq(\text{Na})$ / MHz	-7.0497 ^d	-7.0497(7)
$eQq(\text{N})$ / MHz	-3.8761 ^d	-3.8761(5)
rms^e / kHz	15.9	0.9
N^f	129	122

Notes. ^(a) Merged molecular parameters from a fit to the laboratory and IRC +10216 frequencies. ^(b) Molecular parameters derived by Cabezas et al. (2019). ^(c) Numbers in parentheses are 1σ uncertainties in units of the last digit. ^(d) Fixed to the value determined from the laboratory data. ^(e) Standard deviation of the fit. ^(f) Number of transitions included in the fit.

density of $(3.0 \pm 0.6) \times 10^{12} \text{ cm}^{-2}$. The derived rotational temperature agrees well with the value derived for the cold MgC_3N component, $T_{rot} = 15 \pm 2 \text{ K}$ (Cernicharo et al. 2019b). However, the lines of MgC_3N in the 3mm domain, which involve high energy rotational levels, require an additional gas component with a rotational temperature of $34 \pm 6 \text{ K}$.

3.2. Detection of NaCCCN and non detection of AICCCN

The rotational constants of AICCCN and NaCCCN are available from laboratory experiments (Cabezas et al. 2014, 2019). For NaCCCN seven lines were found in our IRC+10216 Q-Band data with frequencies in very good agreement with those predicted from the laboratory measurements. They are shown in Fig. 2 and their line parameters are given in Table 1. Using the IRC+10216 frequencies and those measured in the laboratory (Cabezas et al. 2019), we derive a new set of molecular constants for NaCCCN, using SPFIT (Pickett 1991), which are given in Table 3.

The calculated dipole moment of NaCCCN is 12.9 D, using the same level of theory as for HMgCCCN. The rotational temperature and column density derived for NaCCCN are $13.5 \pm 1.7 \text{ K}$ and $(1.2 \pm 0.2) \times 10^{11} \text{ cm}^{-2}$, respectively.

In spite of the high accuracy of the frequency predictions for AICCCN in the Q band (better than 25 kHz), we failed to detect any of its lines at the predicted frequencies. Assuming an expanding velocity of 14.5 km s^{-1} (Cernicharo et al. 2000), we derive a 3σ upper limit to its column density of $8 \times 10^{11} \text{ cm}^{-2}$.

4. Discussion

It is interesting to compare the abundance derived for HMgCCCN with those derived for other Mg-bearing cyanides detected in IRC +10216. The column densities reported in IRC +10216 for these species are $N(\text{MgNC}) = 1.3 \times 10^{13} \text{ cm}^{-2}$ (Kawaguchi et al. 1993; Cabezas et al. 2013), $N(\text{HMgNC}) = 6 \times 10^{11} \text{ cm}^{-2}$

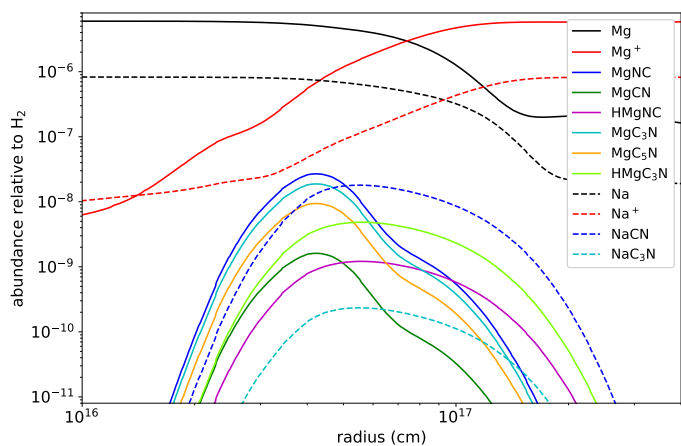
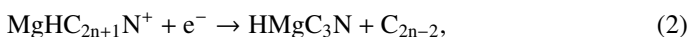


Fig. 3. Abundances calculated with the chemical model for Mg- and Na-bearing cyanides in IRC +10216. The initial abundance of Mg and the branching ratios of the dissociative recombination of metal-bearing cation complexes are chosen to reproduce the observed values. For example, the observed column density of MgNC is $1.3 \times 10^{13} \text{ cm}^{-2}$ (Cabezas et al. 2013) while the calculated value, evaluated as twice the radial column density, is $1.1 \times 10^{13} \text{ cm}^{-2}$. Closed shell species, such as HMgNC, HMgC₃N, NaCN, and NaC₃N, extend further than open shell ones because we assume that they do not react with H atoms and electrons.

(Cabezas et al. 2013), $N(\text{MgCN}) = 7.4 \times 10^{11} \text{ cm}^{-2}$ (Ziurys et al. 1995; Cabezas et al. 2013), $N(\text{MgCCCN}) = 9.3 \times 10^{12} \text{ cm}^{-2}$ (Cernicharo et al. 2019b), and $N(\text{MgC}_3\text{N}) = 4.7 \times 10^{12}$ (Pardo et al. 2021). Therefore, HMgCCCN is just three times less abundant than MgCCCN, in contrast with the smaller hydromagnesium analogue HMgNC, which is 20 times less abundant than MgNC.

In the case of sodium the number of Na-bearing cyanides detected in IRC +10216 is much smaller than for magnesium. The only such species detected in IRC +10216, apart from NaCCCN, is NaCN, which was first detected in IRC +10216 by Turner et al. (1994) and later on mapped by Guélin et al. (1997). Unlike most metal-bearing cyanides detected in IRC +10216, which are most likely formed in the outer layers, NaCN is formed in the inner regions. The studies by Agúndez et al. (2012) and Quintana-Lacaci et al. (2017) constrain the abundance of NaCN to $(3-9) \times 10^{-9}$ relative to H₂, which implies that it is significantly more abundant than NaCCCN, as discussed below.

To shed light on the formation mechanism of HMgCCCN and NaCCCN in IRC +10216 we expanded the chemical model presented in Pardo et al. (2021). The chemical scheme, based on the work of Petrie (1996) and Dunbar & Petrie (2002), starts with the injection of neutral metal atoms into the expanding wind. These atoms are then ionized by the interstellar radiation field and the resulting ionized metal atoms associate radiatively with long neutral carbon chains to form cationic complexes which then recombine dissociatively with electrons to yield neutral fragments as products that are detected in IRC +10216. The formation scheme of HMgCCCN is:



where $n = 2, 3, 4$ and the second reaction yields also other Mg-bearing neutral fragments in addition to HMgCCCN. For Mg we

adopted an initial abundance of 3×10^{-6} relative to H, which allows to reproduce the observed column densities of Mg-bearing molecules, while for Na we adopted an abundance of 4.2×10^{-7} relative to H, as measured in the outer layers of IRC +10216 by Mauron & Huggins (2010). The radiative association rate coefficients for ionized metal atoms and carbon chains are taken from the calculations of Dunbar & Petrie (2002). The other critical input data in the chemical model are the branching ratios yielding the different fragments upon dissociative recombination of the cationic complexes. These ratios are not known and are difficult to predict. We therefore tuned them to reproduce the relative abundances of metal-bearing molecules observed in IRC +10216.

The results from the chemical model are shown in Fig. 3. The calculated abundances of Mg-bearing cyanides are relatively high, in the range 10^{-9} - 10^{-8} relative to H₂. In the case of sodium, we assumed that the main channel in the dissociative recombination of $\text{NaHC}_{2n+1}\text{N}^+$ yields NaCN, while NaCCCN is formed with a branching ratio of $\sim 1\%$. Under this assumption, the column density of NaCCCN agrees with the observed one and NaCN is predicted to have an abundance of $\sim 10^{-8}$ relative to H₂, within the range of values derived by Agúndez et al. (2012) and Quintana-Lacaci et al. (2017). Therefore, the observed abundance of NaCCCN is consistent with NaCN being around 100 times more abundant than it and with Na being injected into the expanding envelope with the abundance constrained by the observations of Mauron & Huggins (2010).

5. Conclusions

We reported the first identification in space of two new metal-bearing carbon chains, HMgCCCN and NaCCCN, toward IRC +10216, the carbon-rich circumstellar envelope of CW Leo. The detection of HMgCCCN adds to the long list of Mg-bearing molecules already known to be present in IRC +10216. On the other hand, the detection of NaCCCN implies that long carbon chains containing metals other than magnesium are also formed in IRC +10216, which opens the door for future detections of carbon chains containing metals such as Na, Al, K, Fe, or Ca.

Acknowledgements. We thank ERC for funding through grant ERC-2013-SyG-610256-NANOCOSMOS. We also thank Ministerio de Ciencia e Innovación of Spain (MICIU) for funding support through projects PID2019-106110GB-I00, PID2019-107115GB-C21 / AEI / 10.13039/501100011033, and PID2019-106235GB-I00.

References

- Agúndez, M., Fonfría, J. P., Cernicharo, J., et al. 2012, *A&A*, 543, A48
 Agúndez, M., Cernicharo, J., Guélin, M., 2014, *A&A*, 570, 45A
 Cabezas, C., Cernicharo, J., Alonso, J. L., et al., 2013, *ApJ*, 775, 133
 Cabezas, C., Barrientos, C., Largo, A., et al. 2014, *J. Chem. Phys.*, 141, 104305
 Cabezas, C., Barrientos, C., Largo, A., et al. 2019, *J. Chem. Phys.*, 151, 054312
 Cernicharo, J. 1985, Internal IRAM report (Granada: IRAM)
 Cernicharo, J., Guélin, M., 1987, *A&A*, 183, L10
 Cernicharo, J., Guélin, M., & Kahane, C. 2000, *A&AS*, 142, 181
 Cernicharo, J., 2012, in *ECLA 2011: Proc. of the European Conference on Laboratory Astrophysics*, EAS Publications Series, 2012, Ed.: C. Stehl, C. Joblin, & L. d'Hendecourt (Cambridge: Cambridge Univ. Press), 251; https://nanocosmos.iff.csic.es/?page_id=1619
 Cernicharo, J., Teyssier, D., Quintana-Lacaci, G., et al., 2014, *ApJ*, 796, L21
 Cernicharo, J., Marcelino, N., Agúndez, M., Guélin, M., 2015, *A&A*, 575, A91
 Cernicharo, J., Velilla-Prieto, L., Agúndez, M., et al., 2019a, *A&A*, 627, L4
 Cernicharo, J., Cabezas, C., Pardo, J.R. et al., 2019b, *A&A*, 630, L2
 Cernicharo, J., Marcelino, N., Agúndez, M. et al. 2020a, *A&A*, 642, L8
 Cernicharo, J., Marcelino, N., Pardo, J.R. 2020b, *A&A*, 641, L9
 Cernicharo, J., Agúndez, M., Kaiser, R., et al. 2021a, *A&A*, 652, L9
 Cernicharo, J., Cabezas, C., Agúndez, M., 2021b, *A&A*, 648, L3

- Cernicharo, J., Fuentetaja, R., Agúndez, M., et al. 2022, A&A, 663, L9
- Cernicharo, J., Pardo, J.R., Cabezas, C. et al. 2023, A&A, 670, L19
- Changala, P.B., Gupta, H., Cernicharo, J. et al. 2022, ApJ, 940, L42
- Dunbar, R. C. & Petrie, S. 2002, ApJ, 564, 792
- Giesen, T.F., Harding, M.E., Gauss, J., et al. 2020, J. Mol. Spectrosc., 371, 111303
- Ginsburg, A., McGuire, B., Plambeck, R. et al. 2019, ApJ, 872, 54
- Gordon, V.D., Nathan, S.E., Apponi, A.J. et al. 2000, J. Chem. Phys., 113, 5311
- Guélin, M., Lucas, R., & Cernicharo, J. 1993, A&A, 280, L19
- Guélin, M., Lucas, R., & Neri, R. 1997, in CO: Twenty-Five Years of Millimeter Wave Spectroscopy, eds. W. B. Latter et al. (Dordrecht: Kluwer), IAU Symp., 170, 359
- Hill, J. G., Mazumder, S., Peterson, K. A., 2010, J. Chem. Phys., 132, 054108
- Hirahara, Y., Ohshima, Y. & Endo, Y. 1993, ApJ, 408, L113
- Kawaguchi, K., Kagi, E., Hirano, T., et al., 1993, ApJ, 406, L39
- Knizia, G., Adler, T. B., Werner, H.-J., 2009 J. Chem. Phys. 130, 054104
- Lucas, R., & Guélin, M. 1990, in Submillimetre Astronomy, ed. G. D. Watt & A. S. Webster (Dordrecht: Kluwer), 97
- Mauron, N., Huggins, P.J., 2010, A&A, 513, A31
- McCarthy, M.C., Gottlieb, C.A., Gupta, H. & Thaddeus, P. 2006, ApJ, 652, L141
- Müller, H.S.P., Schlöder, F., Stutzki, J., Winnewisser, G. 2005, J. Mol. Struct., 742, 215
- Ohishi, M., Kaifu, N., Kawaguchi, K. et al. 1989, ApJ, 345, L83
- Pardo, J. R., Cernicharo, J., & Serabyn, E. 2001, IEEE Trans. Antennas and Propagation, 49, 12
- Pardo, J. R., Cernicharo, J., Velilla Prieto, L., et al., 2018, A&A, 615, L4
- Pardo, J. R., Bermúdez, C., Cabezas, C., et al. 2020, A&A, 640, L13
- Pardo, J. R., Cabezas, C., Fonfría, J.P. et al. 2021, A&A, 652, L13
- Pardo, J. R., Cernicharo, J., Tercero, B. et al. 2022, A&A, 658, A39
- Petrie, S. 1996, MNRAS, 282, 807
- Pickett, H. M. 1991, J. Mol. Spectrosc., 148, 371
- Pickett, H.M., Poynter, R. L., Cohen, E. A., et al. 1998, J. Quant. Spectrosc. Radiat. Transfer, 60, 883
- Pulliam, R. L., Savage, C., Agúndez, M., et al. 2010, ApJ, 725, L181
- Quintana-Lacaci, G., Cernicharo, J., Velilla Prieto, L., et al. 2017, A&A, 607, L5
- Tachibana, S., Kamizuka, T., Hirota, T., et al. 2019, ApJ, 875, L29
- Tercero, F., López-Pérez, J. A., Gallego, et al. 2021, A&A, 645, A37
- Turner, B., Steimle, T.C., and Meerts, L., 1994, ApJ, 426, L97
- Umeki, H., Nakajima, M. & Endo, Y. 2014, J. Chem. Phys., 141, 184303
- Werner, H.-J., Knowles, P. J., Knizia, G., et al., 2020, MOLPRO, version 2020.2
- Zack, L. N., Halfen, D. T., & Ziurys, L. M., 2011, ApJ, 733, L36
- Ziurys, L. M., Apponi, A. J., Guélin, M., & Cernicharo, J. 1995, ApJ, 445, L47
- Ziurys, L. M., Savage, C., Highberger, J. L., et al. 2002, ApJ, 564, L45